SUPPLEMENTARY INFORMATION

Nanoclusters of crystallographically aligned nanoparticles for magnetic thermotherapy: aqueous ferrofluid, agarose phantom and ex vivo melanoma tumour assessment.

D. Coral, P. A. Soto, V. Blank, A. Veiga, E. Spinelli, S. Gonzalez, G.P. Saracco, M.A. Bab, D. Muraca, P.C.Setton-Avruj, A. Roig, L. Roguin, M. B. Fernández van Raap

S1: M vs. H data fitting procedure.

The magnetization (M) field (H) dependence were fitted using the Langevin function[1] $L(\mu,H) = N\mu\left[Coth\left(\frac{\mu H}{k_B T}\right) - \frac{k_B T}{\mu H}\right]$ and a LogNormal distribution of magnetic moments $g(\mu) = \frac{1}{\mu\sigma_\mu\sqrt{2\pi}} exp\left[\frac{-ln^2(\mu/\mu_0)}{2\sigma_\mu^2}\right]$ plus a high field susceptibility (χ) lineal term as:

$$M(H) = \int_0^\infty L(\mu,H)g(\mu)d\mu + \chi H \qquad (1)$$

Fitted parameters were the specific number of nanoclusters N, standard deviation (σ_μ) of $ln(\mu/\mu_0)$, median magnetic moment (μ_o).

From fitted values the mean moment $\mu_m = \mu_o exp\left[\sigma_\mu^2/2\right]$ and the saturation magnetization $M_s = N\mu_m$ were derived and values are listed in Table 2.

S2: SAR semi-empirical calculations.

For an assembly of randomly oriented single-domain magnetic nanoparticles, exhibiting thermally activated coherent magnetization reversal, the specific absorption rate (SAR) parameter is given within the lineal response approximation[2] and Stoner-Wohlfarth (SW) theory[3] by:

$$SAR = \mu_0 \pi f H_0^2 \int_0^\infty \chi''(f,\tau) g(\tau) d\tau$$

with $\chi''(f,\tau) = \frac{2\pi f\tau}{1+(2\pi f\tau)^2}\chi_0$

where $g(\tau)$ is the relaxation time distribution due to nanoparticles size distribution, aggregation and dipolar interactions. At low field amplitude, χ_0, can be approximated by the dc initial specific susceptibility[4]and modelled as $\chi_0 \cong \frac{\mu_0 \rho M_s^2 V}{3k_B T}$.

The magnetization reverses in coherent way due to Néel or Brown processes. Brown relaxation times depend on medium viscosity η and hydrodynamic volume V_H as $\tau_B = \frac{3\eta V_H}{k_B T}$. The Néel relaxation time for uniaxial anisotropy depends on the energy barrier U of a double-well potential and on the inverse attempt frequency[5] $\tau_0 \sim 10^{-13}$ - 10^{-10} s as $\tau_N = \tau_0 \exp(U/k_B T)$. The dynamic of the particle's dipole moment is governed by the effective relaxation time τ, given by $\tau^{-1} = \tau_N^{-1} + \tau_B^{-1}$. For independent relaxation modes[6] the faster occurs. Néel mechanism is inhibited ($\tau_N \gg \tau_B$) when the particles are large and/or have large magnetic anisotropy. Brown relaxation is inhibited ($\tau_N \ll \tau_B$) when the particles display large hydrodynamic volume.

By this way, SAR theoretical calculation[4] can be carried out as:

$$SAR(U) = \mu_0 \pi f H_0^2 \int_0^\infty \chi''(f,U) g(U) dU \qquad (2)$$

Where μ_0 is the permeability of free space (4π x 10^{-7} H m^{-1}) and $g(U)$ in the energy barrier distribution of mean value $<U>$.

Also, for this assembly of nanoparticles the mean energy barrier can be independently determined from the coercive field (H_c) temperature dependence[7] by fitting the equation:

$$H_c = 0.96 \frac{\langle U \rangle}{\mu_0 \mu} \left[1 - \left(\frac{k_B T \ln\left(\tau_m / \tau_0\right)}{\langle U \rangle} \right)^{1/2} \right] \qquad (3)$$

where μ is the nanoparticles magnetic moment and the measuring time $\tau_m \sim 100$ s for d.c. magnetometry.

By this way, using equation (2), the magnetic and structural parameters and the $\langle U \rangle$ values determined from the fit of H_c *vs.* T measurements with equation (3), SAR can be calculated[8].

We have applied this procedure to calculate the SAR of our nanocluster aqueous suspensions using the magnetic and structural data listed in tables 1 and 2. The so-calculated SAR values are in good agreement with those calorimetrically determined at 100 kHz and 9.3 kA m^{-1}. This result reinforce the idea that these nanoclusters, composed of crystallographically aligned nanoparticles, behaves as single magnetic domain.

S3: Supplementary Figures:

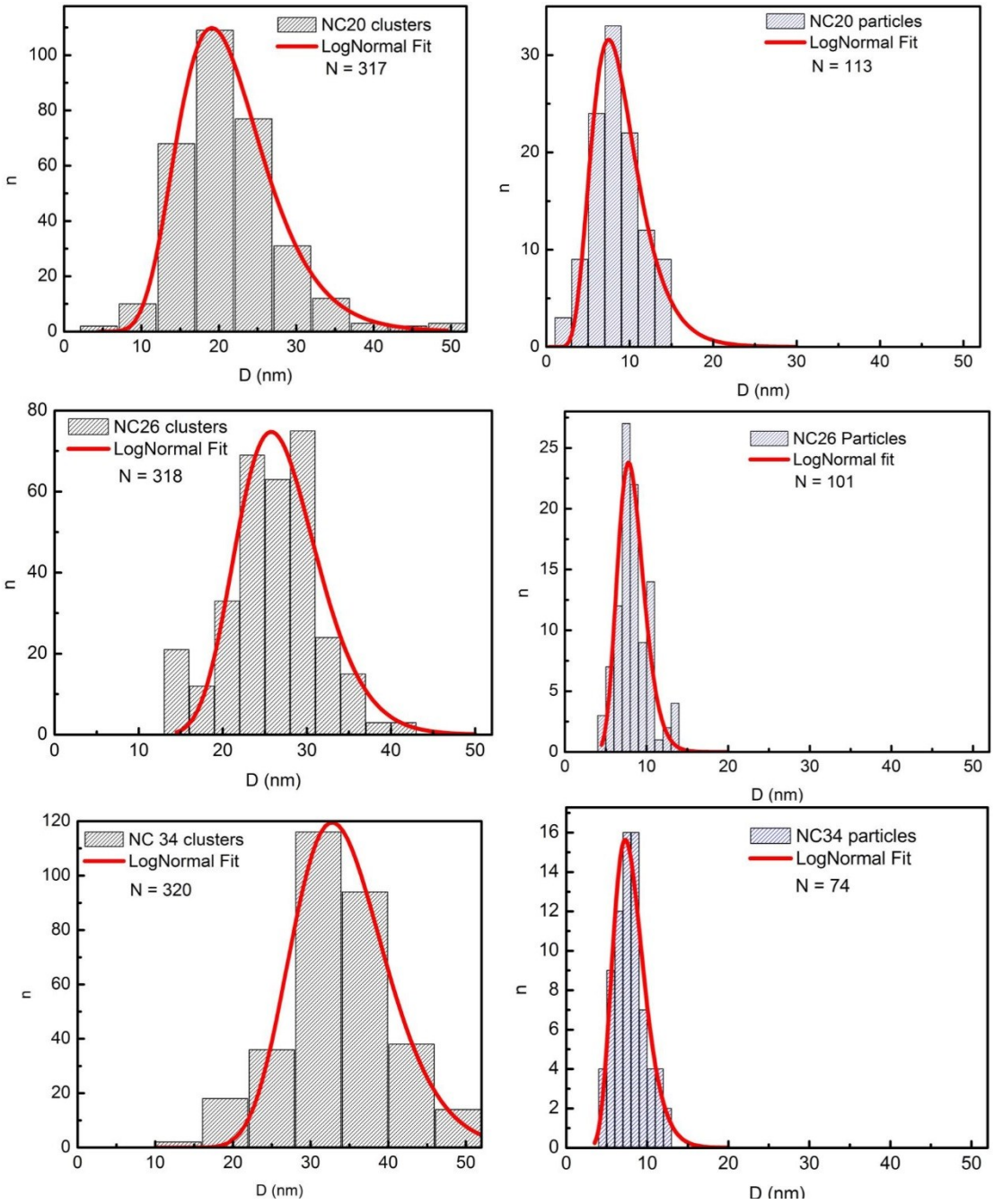

Figure S1. Size (*D*) histograms retrieved from TEM images of nanoclusters and nanoparticles inside NCs. Continuous lines represent LogNormal fits. *N* stands for the number of counted objects for constructing the histograms.

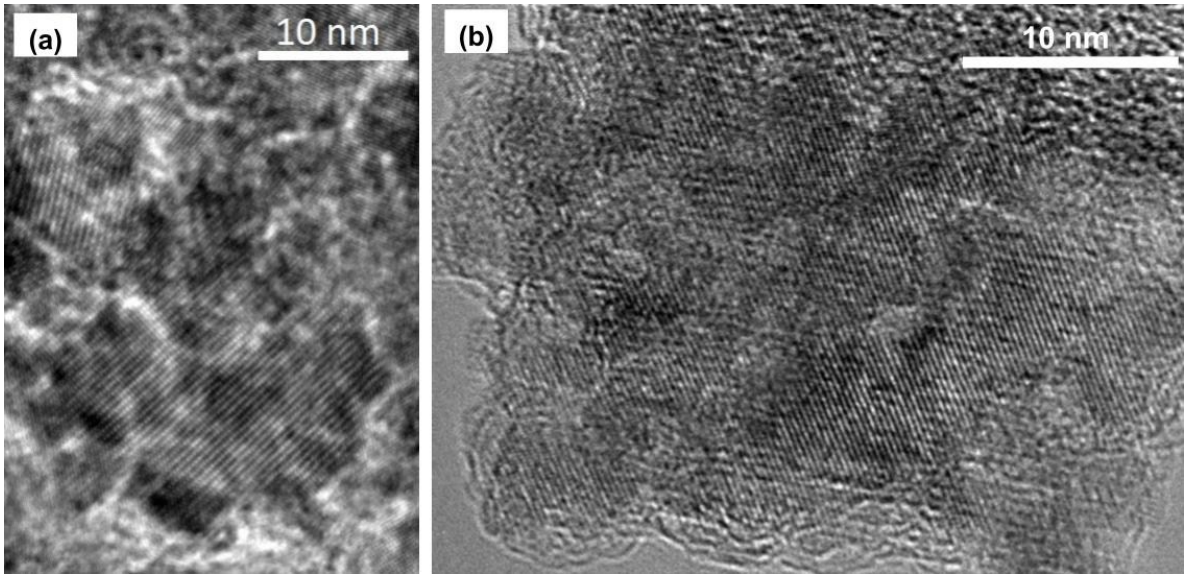

Figure S2 .TEM images for sample NC27 where interface among particles inside the nanocluster is observed.

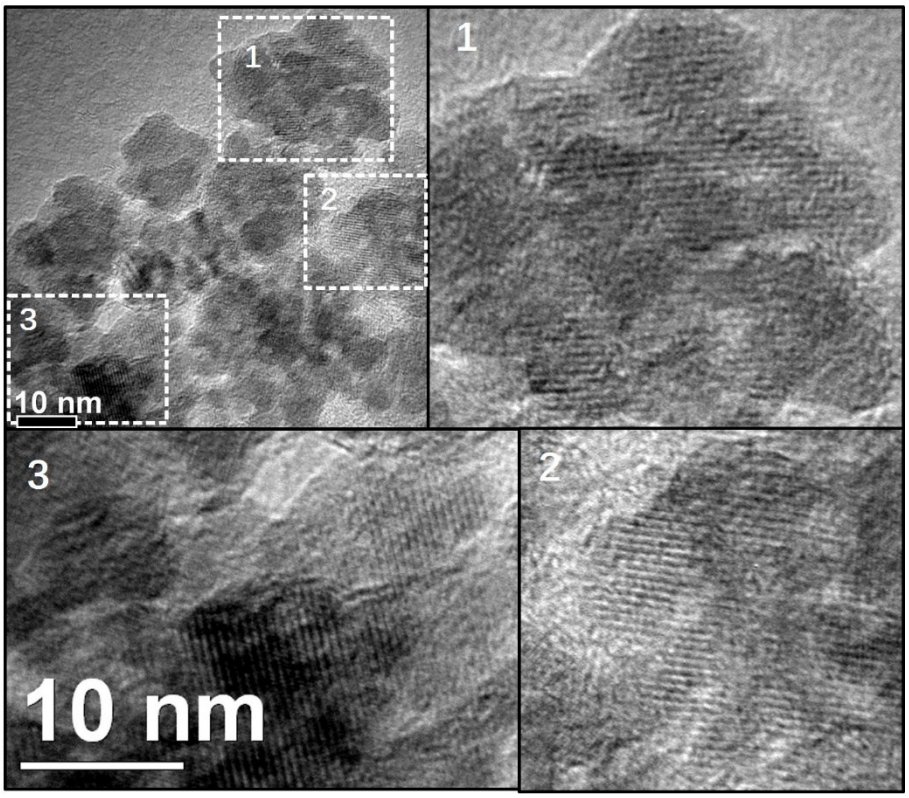

Figure S3. HR-TEM of NC26 sample. A zoom of three NCs enclosed by white box are shown in panels 1, 2 and 3. These NCs were selected to show in more detail the crystallographic alignment of their nanoparticles.

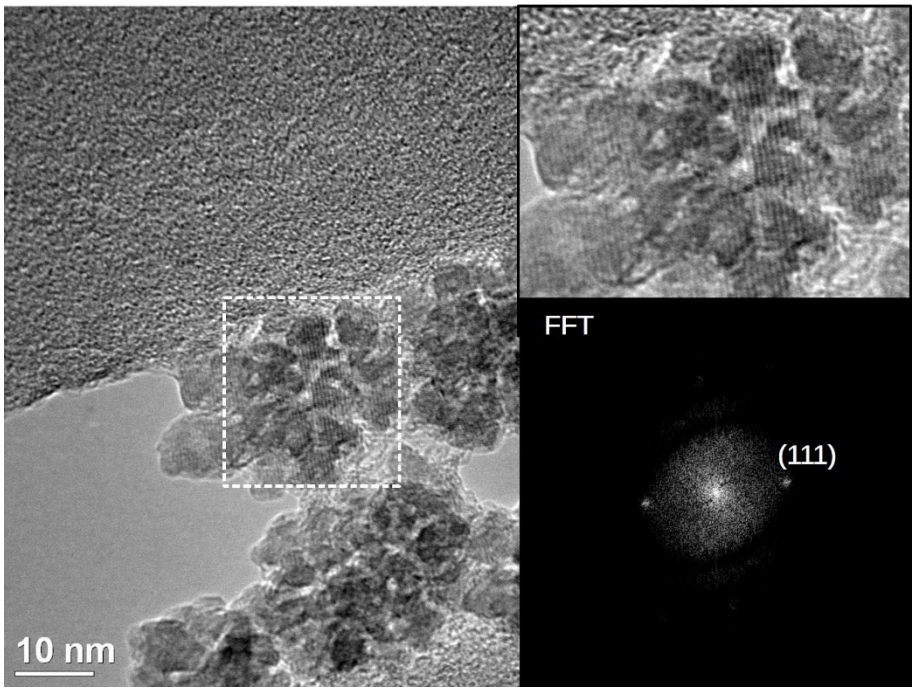

Figure S4. HRTEM of NC26. A zoom of the NC enclosed by a white box is shown in left top panel where crystallographic alignment can be clearly observed. Fast Fourier transformation (FFT) of this NC confirm the crystallographic alignment between MNPs on the NC.

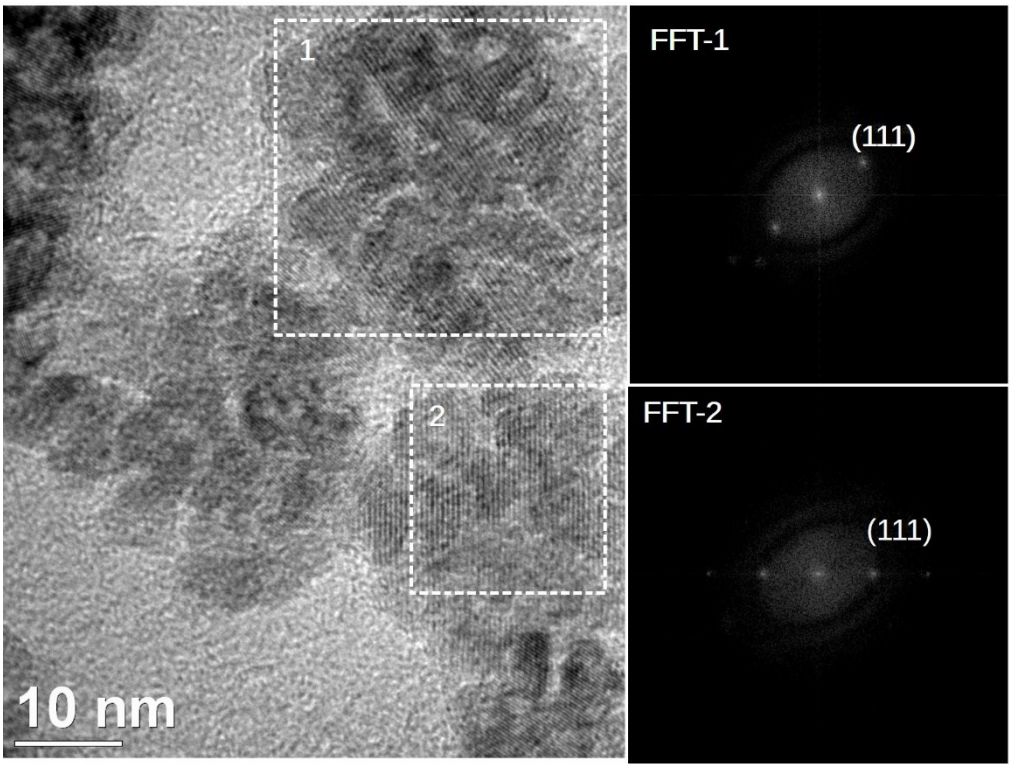

Figure S5. HRTEM of NC26. Fast Fourier transformation (FFT) of the areas inside the white boxes shows crystallographic alignment between MNPs on each NC (Left panels).

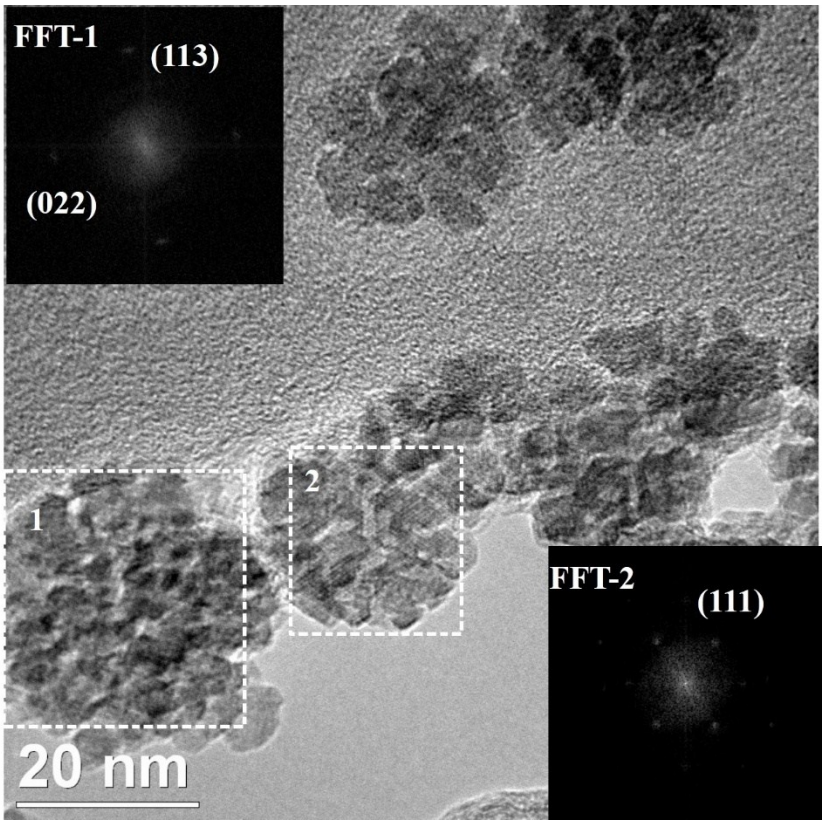

Figure S6. HRTEM of NC26. Fast Fourier transformation (FFT) of the areas inside the white boxes shows crystallographic alignment between MNPs on each NC.

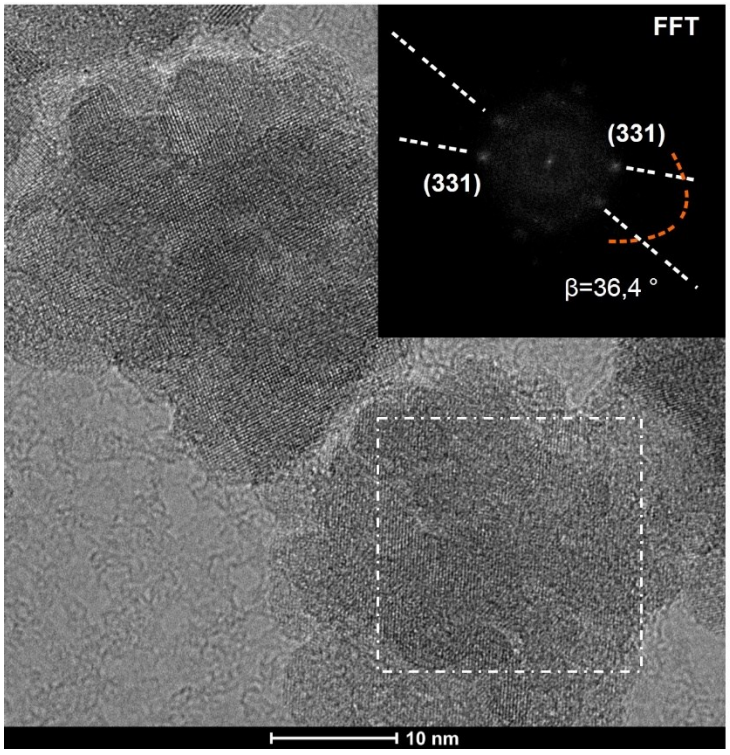

Figure S7. HR-TEM of two NCs Inset shows the Fast Fourier transform (FFT) of the one enclosed by a white box showing two orientations of the same crystallographic plane.

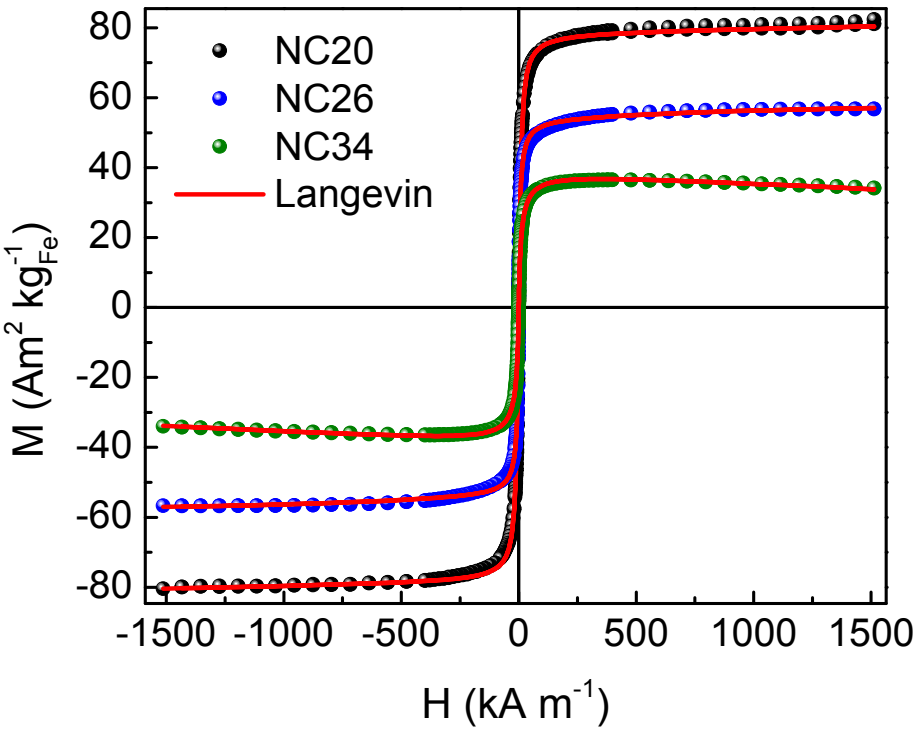

Figure S8. Magnetization curves NC aqueous suspensions listed in Table 2 measured at 300 K. Continuous red lines stand for curve fitting using the Equation1.

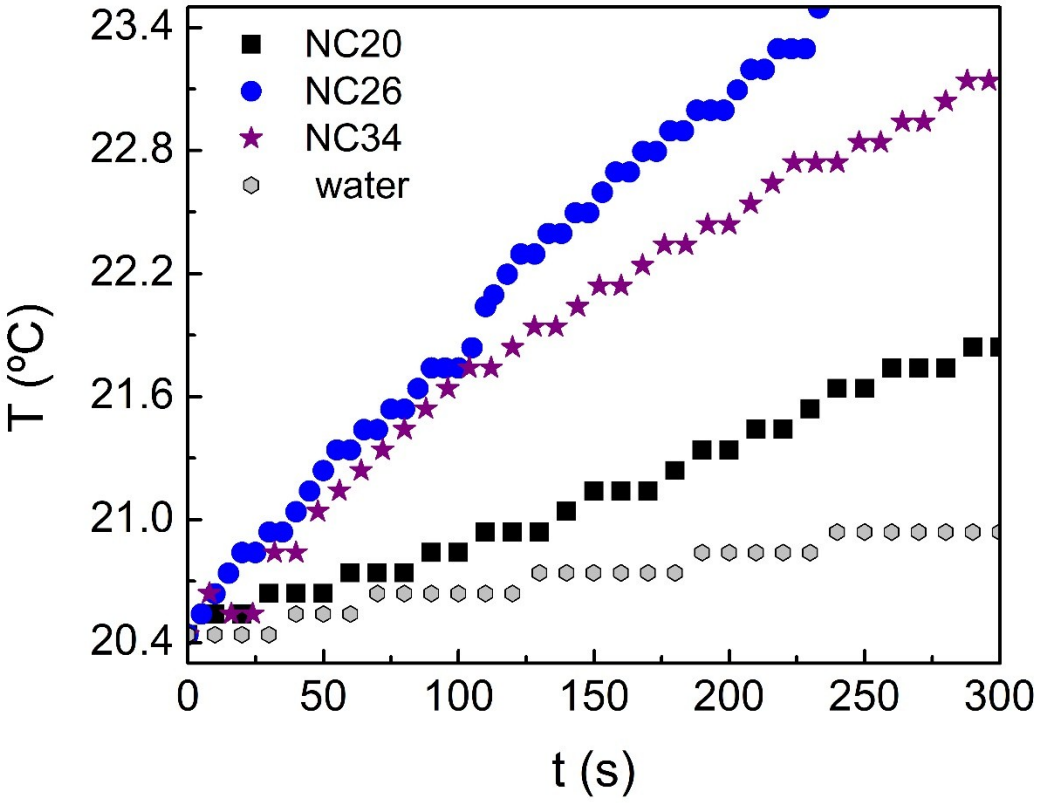

Figure S9. Heating curves of NC aqueous suspensions listed in Table 2 obtained at 100 kHz and 9.3 kA m^{-1}.

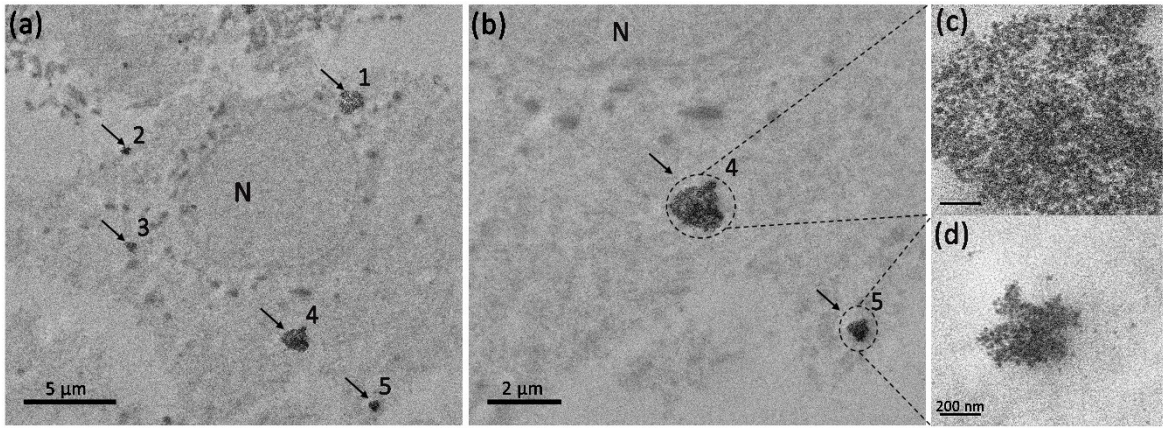

Figure S10. Cryo TEM of B16-F0 cell incubated with NCs for 17 h showing the cytosolic localization of NPs incorporated in endosome-like structures (b) higher resolution image of endosome-like structures 4 and 5. (c) Detail of NCs organization inside endosome-like 4, (d) detail of NCs organization inside endosome-like 5. N: nucleus **arrows** show NPs incorporated in endosome-like structures

S3: Field inductor design.

Commercial equipment for inducting heating can be adapted for magnetic hyperthermia experiments. These devices, originally intended for metal melting, demand high electric power and require water-cooling techniques, being large, heavy and thus, not portable. This is a complication, since in vivo test are often carried out in biology and medicine

schools and even in health centres where bioethical regulations are satisfied. Therefore, it is extremely advantageous to have a robust and small size applicator that can be transported without requiring specialized installation. With this objective in mind, a portable applicator was designed as a practical tool for in vivo, in vitro and material assays.

The device can hold a Dewar for materials testing, a Petri dish with in vitro culture or a stretcher for mice treatment. The magnetic field is produced by imposing a high current in a coil housing the animal or the sample to test. This is efficiently done by composing a resonant network with the coil and an extra capacitor C, as is usual in magnetic field generators for induction heating[9].

During magnetic hyperthermia applications, coil copper losses are dominant and its transfer to the sample must be avoid. In order to circumvent water-cooling, coil design was carefully optimized to reduce Joule heating. The proposed geometry minimizes the current needed to obtain the required magnetic field, so the copper pipe, mandatory for water-cooled devices, can be replaced by a multistrand Litz wire. The conductor used for the resonant inductor is composed of 40 glazed copper wires of 0.25 mm diameter, resulting in a wire of an overall diameter of approximately 2 mm. The coil was built with 35 wire turns on a cylindrical acrylic support of 55 mm of inner diameter (3 mm wall). The housing total volume is 170 cm^3, with 70 cm^3 of uniform field and the resulting coil inductance L= 47.6 μH with a quality factor (Q) of 234 at 100 kHz (this implies a resistance R less than 0.12 Ω).In order to obtain an operating frequency of 100 kHz, a capacitor of C=50 nF is required. It is important to note that the capacitor must be able to handle the current flowing through the inductor (up to 20 A) and also the voltage that this current imposes on the resonant circuit (up to 700 VRMS). A commercial CELEM CSPI20/200 (1000 VRMS, 200 ARMS) capacitor was used. A general scheme of the applicator electronics is shown in Figure S3. The device is powered directly from power line (220V, 50Hz) that is rectified and filtered to produce an unregulated 310 VDC voltage bus. This direct-current voltage is converted to a 100 kHz square wave by full-bridge inverter[10] that is applied to the resonant network through an isolation transformer. High operating frequency allows the use of ferrite core and results in a low volume and reduced weight solution: two desired features for a portable device. The magnetic field is sensed by an additional single turn coil that probes amplitude, frequency and phase. A digital CPLD (Complex Programmable Logic Device) Xilinx CoolRunner-II uses this information to produce the required control signals for the inverter, in order to keep operation at the resonance frequency of the network and to control the magnetic field intensity.

The capacitor and the resonant coil were mounted using copper bars and carefully isolated from the rest of the equipment.

A fan with a nozzle is enough to keep the housing temperature below room temperature ±2 °C.

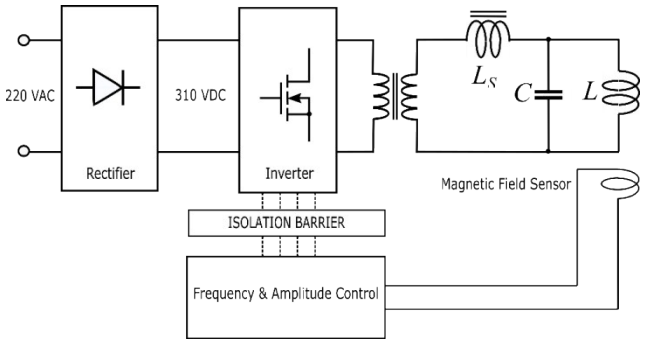

Figure S11. Block diagram of the electronic components of the applicator. The LLC network is kept at resonant frequency by an AC/AC converter coupled through a transformer. Magnetic field is sensed by a single turn coil and controlled by a digital system

References:

1 C. P. Bean and J. D. Livingston, *J. Appl. Phys.*, 1959, **30**, S120–S129.

2 J. Jensen and A. R. Mackintosh, *Rare Earth Magnetism: Structures and Excitations*, CLARENDON PRESS, Oxford, 1991.

3 E. C. Stoner and E. P. Wohlfarth, *Philos. Trans. R. Soc. London. Ser. A, Math. Phys. Sci.*, 1948, **240**, 599–642.

4 R. E. Rosensweig, *J. Magn. Magn. Mater.*, 2002, **252**, 370–374.

5 J. L. Dormann, L. Bessais and D. Fiorani, *J. Phys. C Solid State Phys.*, 1988, **21**, 2015.

6 M. I. Shliomis and V. I. Stepanov, in *Advances in Chemical Physics: Relaxation Phenomena in Condensed Matter*, ed. W. Coffey, John Wiley & Sons, Inc., Hoboken, NJ, USA, 2007, pp. 1–30.

7 W. C. Nunes, W. S. D. Folly, J. P. Sinnecker and M. A. Novak, *Phys. Rev. B*, 2004, **70**, 14419.

8 M. B. Fernández van Raap, D. F. Coral, S. Yu, G. A. Muñoz, F. H. Sánchez and A. Roig, *Phys. Chem. Chem. Phys.*, 2017, **19**, 7176–7187.

9 O. Lucia, P. Maussion, E. J. Dede and J. M. Burdio, *IEEE Trans. Ind. Electron.*, 2014, **61**, 2509–2520.

10 S. A. Gonzalez, E. M. Spinelli, A. L. Veiga, D. F. Coral, M. B. F. van Raap, P. M. Zelis, G. A. Pasquevich and F. H. Sanchez, in *2017 IEEE 8th Latin American Symposium on Circuits & Systems (LASCAS)*, IEEE, 2017, pp. 1–4.